nature energy

Article

https://doi.org/10.1038/s41560-023-01414-5

Origin of fast charging in hard carbon anodes

Received: 1 March 2022

Accepted: 6 November 2023

Published online: 03 January 2024

Check for updates

Yuqi Li[1,2,7], Alexandros Vasileiadis[3,7], Quan Zhou[1,4,7], Yaxiang Lu[1,5] ✉, Qingshi Meng[1,4], Yu Li[1,2], Pierfrancesco Ombrini[3], Jiabin Zhao[1,4], Zhao Chen[1,2], Yaoshen Niu[1], Xingguo Qi[1,4], Fei Xie[1], Remco van der Jagt[3], Swapna Ganapathy[3], Maria-Magdalena Titirici[6], Hong Li[1,2], Liquan Chen[1,2], Marnix Wagemaker[3] ✉ & Yong-Sheng Hu[1,2,4,5] ✉

Transport electrification and grid storage hinge largely on fast-charging capabilities of Li- and Na-ion batteries, but anodes such as graphite with plating issues drive the scientific focus towards anodes with slopped storage potentials. Here we report fast charging of ampere-hour-level full Na-ion batteries within about 9 minutes for continuous 3,000 cycles based on hard carbon anodes. These anodes, in addition to displaying a sloped storage voltage, provide capacity at a nearly constant voltage just above the plating potential, without observing Na-metal plating under high areal capacity. Comparing the electrochemical behaviour of Li and Na in hard carbon through experimental and computational techniques, a unified storage mechanism relying on the dimensions of wedge nanopores and drawing parallels with underpotential deposition for metals is brought forward, providing a rational guide for achieving fast storage in hard carbon anodes.

The unsatisfactory power density of rechargeable batteries causes the recharging time of electric vehicles to be much longer than the refuelling time of internal combustion engine cars[1–5]. The anode side is widely believed to be the bottleneck for achieving fast charging[6]. For example, the standard graphite anode for commercial Li-ion batteries (LIBs) suffers from Li plating during fast charging, which accelerates battery degradation and induces safety issues. Because of the low Li storage potential plateau (~0.1 V versus Li/Li^+), even small overpotentials due to limited Li-ion kinetics can initiate plating[7]. To solve this issue, a series of advanced anode materials such as graphene–Nb_2O_5 composites[8], $Nb_{16}W_5O_{55}$[9], black phosphorus–graphite composites[10] and $Li_{3+x}V_2O_5$[11], demonstrating good kinetics have been proposed, all relying on a sloping voltage profile that is typically associated with superior kinetics.

Hard carbons with tunable structure and low reaction strain have been applied for some high-power-type LIBs to excavate the high-power potential, delivering 82% capacity retention at 6 C after 500 cycles in pouch cells[12]. Hard carbons with good comprehensive performance are also promising anode choices[13,14] for Na-ion batteries (NIBs)[15–17]. Although previous work showcased that the use of small-sized pouch cells (<0.01 Ah) with limited areal capacity (~1.3 mAh cm^{-2}) and lifetime (~100 cycles) can demonstrate fast charging[18], there has been no report on fast-charging NIBs based on Ah-level cells with thick hard carbon anodes up to now. Achieving a long cycling life with high areal capacity under high rates is particularly challenging.

The simultaneous existence of sloping and plateau regions in the sodiation voltage response (Supplementary Fig. 1) is often considered challenging to enable high-power applications in practical large-sized NIBs. Further, clarifying the relationship between the complex carbon structure, storage mechanism and fast-charging performance of alkali-metal ion batteries has so far proved inconclusive[19,20]. Despite Li and Na storage in hard carbons having been reported[21–24], most previous work investigated the Li and Na storage behaviour separately.

[1]Key Laboratory for Renewable Energy, Beijing Key Laboratory for New Energy Materials and Devices, Beijing National Laboratory for Condensed Matter Physics, Institute of Physics, Chinese Academy of Sciences, Beijing, China. [2]College of Materials Science and Optoelectronic Technology, University of Chinese Academy of Sciences, Beijing, China. [3]Department of Radiation Science and Technology, Delft University of Technology, Delft, Netherlands. [4]HiNa Battery Technology Co. Ltd., Beijing, China. [5]Huairou Division, Institute of Physics, Chinese Academy of Sciences, Beijing, China. [6]Department of Chemical Engineering, Imperial College London, London, UK. [7]These authors contributed equally: Yuqi Li, Alexandros Vasileiadis, Quan Zhou. ✉e-mail: yxlu@iphy.ac.cn; m.wagemaker@tudelft.nl; yshu@iphy.ac.cn

https://doi.org/10.1038/s41560-023-01414-5

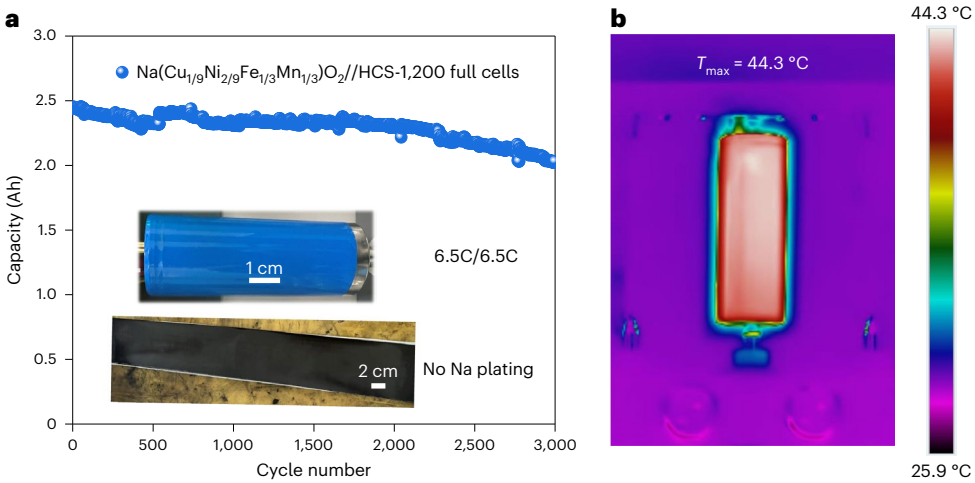

Fig. 1 | Ultrafast NIBs. a, Cycling performances of $Na(Cu_{1/9}Ni_{2/9}Fe_{1/3}Mn_{1/3})O_2$//HCS-1,200 NIBs at a current rate of 6.5 C (insets: the digital pictures of the 26700-type cylindrical cell and its anode after 3,000 cycles). **b**, Surface temperature distribution of NIBs during fast charging at ambient temperature.

An in-depth quantitative parallel analysis may provide a deeper understanding of the structure–performance relationship.

In this work, the superior fast-charging performance and long cycling life of Ah-level Na-ion cylindrical cells with hard carbon anodes is demonstrated. Through simultaneous investigation of the Li and Na storage in hard carbons via cross validation and quantitative analysis, the origin of fast-charging NIBs with hard carbon anodes is unravelled, where a unified Li and Na storage mechanism of adsorption pore filling is proposed to address the mechanistic debates and the underpotential deposition (UPD)-like storage process rationalizes the excellent kinetics of carbon anodes. Moreover, utilizing nanoscale and mesoscale simulations to evaluate critical thermodynamic and kinetic properties, the observed potential gap (30 to 40 mV) in the plateau region between Li and Na is interpreted by the interface energy difference between Li/Na and hard carbon. This work brings insight to understand the Li and Na storage behaviour in hard carbon anodes and provides universal structure design principles to tune their microstructures for further performance improvement.

Fast-charging capability of hard carbon anodes

Here we choose specific hard carbon spheres (HCSs) (Supplementary Fig. 2) as a model system to study the origin of fast-charging properties. Two different carbonization temperatures (1,200 and 1,600 °C) were adopted to tune the microstructures of HCSs. Comprehensive characterizations (Supplementary Figs. 2–8) reveal that the increase of graphitic layer ordering and closed pore volume, and the decrease in defect concentration and CO_2 specific area with increasing carbonization temperature, all align with findings reported in the literature[14,25,26].

Fast-charging/discharging tests for the large-format NIBs (26700-type cylindrical cells), utilizing the layered O3-$Na(Cu_{1/9}Ni_{2/9}Fe_{1/3}Mn_{1/3})O_2$ cathode[27] and HCS anode, were performed. The HCS-1,200-based full cell delivers ~3 Ah at 0.1 C and boosts a high areal capacity of ~2.2 mAh cm^{-2}. It is demonstrated in Fig. 1a that the Na-ion full cell with an HCS-1,200 anode maintains 83% of its capacity after 3,000 cycles at a 6.5 C rate cycling. Even with rapid charge/discharge cycles, taking approximately 9 minutes, no Na precipitation is observed, as confirmed by ex situ optical tests (Supplementary Fig. 9a,b). In Supplementary Fig. 9c, the high average Coulombic efficiency of ~99.93% also indicates the absence of Na precipitation over the 3,000 cycles. More importantly, the highest value of NIB surface temperature during the charging process is only ~44.3 °C due to the small internal resistance (Fig. 1b and Supplementary Fig. 10). Enhanced kinetics can be expected with an increase in temperature, but stable cycling can still be achieved due to the high thermal stability of our NIB system[28–30]. We can speculate that both the sloping and plateau regions of HCS-1,200 have favourable resilience against fast charging, evident from the distinct galvanostatic charge/discharge curves of the full cell under different rates (Supplementary Fig. 11). The HCS-1,600-based full cell also shows a high-capacity retention of 81% after 1,500 cycles and 60% after 3,000 cycles under 6.5 C rate (Supplementary Fig. 12), which is relatively poorer than that of the HCS-1,200. Considering the fast-charging performance, which would be influenced by the kinetics of the cathode, anode and electrolyte of a cell, we deliberately changed the relevant component. It is found that anode side has more pronounced influence on fast-charging performance, which is similar to commercial LIBs with graphite anode[31–34] (Supplementary Fig. 13). The above results underscore the capability of HCSs in realizing fast charging/discharging of NIBs, motivating further in-depth investigations to understand the underlying mechanisms.

We first evaluated the storage behaviours of HCSs for Li and Na in half cells, with the corresponding potential curves shown in Supplementary Figs. 14 and 15 and Fig. 2. The potential decreases sharply upon Li and Na insertion into the HCS matrix (Fig. 2a,b). The capacity in these sloping voltage regions of HCSs for Li and Na storage is summarized in Supplementary Fig. 16. Interestingly, we found that the sloping capacity of Li storage is about 1.8 times that of the Na storage for both HCS-1,200 and HCS-1,600. The 1.8 ratio can be confirmed by the data in previous literature, as shown in Supplementary Fig. 17. Following the sloping region, the potential curve reaches a potential plateau around 0–0.1 V (Li) or 0.15 V (Na).

To obtain an in-depth understanding of the storage mechanism, it is crucial to investigate the voltage curves up to the point where a characteristic 'V' shape is reached (Fig. 2c,d). This feature is caused by the alkali-metal nucleation barrier, indicating the discharge state where the HCSs achieve the maximum reversible capacity. For this reason, overdischarge below 0 V was applied to both Li and Na half cells. For the Li case, a hidden and significant plateau is observed (Fig. 2c) below 0 V versus Li metal, where the capacity improves further by 140 and 441 mAh g^{-1} for HCS-1,200 and HCS-1,600, respectively. In contrast, the capacity below 0 V versus Na/Na^+ only contributes an additional 11 and 18 mAh g^{-1} to Na plateau capacity for HCS-1,200 and HCS-1,600, respectively (Fig. 2b). The above observation reveals that the previously discussed trend—the increase of plateau capacity with a rise in carbonization temperature—applies to both Li and Na systems. Thus, our findings challenge the common viewpoint that hard carbon anodes prepared by high carbonization temperature deliver a higher

https://doi.org/10.1038/s41560-023-01414-5

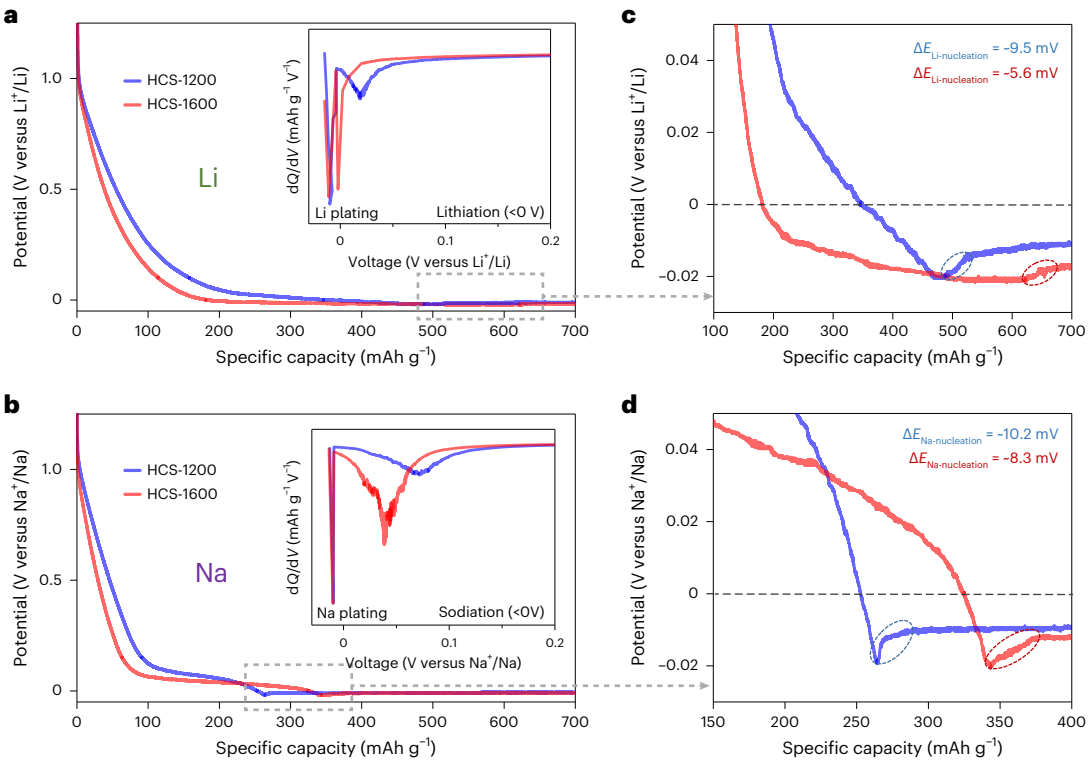

Fig. 2 | Electrochemical behaviours of Li and Na storage in HCSs. a,**b**, Galvanostatic discharge curves (<0 V) at a current rate of 15 mA g^{-1} in LIBs and NIBs, respectively. Inset: related dQ/dV curves. **c**,**d**, Detailed curves below 0 V and the nucleation overpotentials ($\Delta E_{\text{Li-nucleation}}$, Li metal nucleation overpotential; $\Delta E_{\text{Na-nucleation}}$, Na metal nucleation overpotential).

plateau capacity for Na as compared with Li storage because previous reports (Supplementary Fig. 17) overlooked the capacity below 0 V (ref. 22). The reversibility of the Li and Na storage of <0 V is also verified by charging tests in Supplementary Fig. 18. Furthermore, differential capacity (dQ/dV) analysis reveals that completed peaks can be obtained once undergoing overdischarge, and the average reaction potential of the plateau region is lower for Li storage than for Na storage.

Quantitative analysis for sloping region

The sloping region is usually explained as an adsorption or intercalation mechanism by most previous reports[20,35]. In situ Raman tests (Supplementary Fig. 19) revealed that there is no peak splitting of the D or G band, and no new peaks appear, indicating that Li^+ and Na^+ do not intercalate into the layers of carbon[36,37]. The I_D/I_G (the integrated intensity ratio of the D1-band over the G-band) values show nearly no variation in the sloped voltage region for both Li and Na (Supplementary Figs. 20 and 21), suggesting a relatively weak interaction between Li, Na and the HCSs. The following hypothesis is that HCSs anodes provide sloping capacity through adsorption. Several density functional theory (DFT) studies have explored the nature of defect adsorption on vacancies and heteroatoms, revealing various adsorption environments with broad storage potential distributions and rationalizing the sloping voltage region[38]. Herein alkali-metal edge adsorption on graphene is studied with DFT (Fig. 3a,b), which predicts gradually decreasing high-voltage response for both Li and Na, matching the observed behaviour. Both alkali metals utilize the same binding spots, acquiring a zig-zag configuration. However, Li ions can stabilize directly across from each other (Fig. 3b), which is predicted to be unstable for the Na case, indicating that the smaller size of Li allows more storage on the active edges for the same surface.

Experimentally, the ratio of sloping capacity of Li to Na and the ratio of the projected area of Na to Li ions is both 1.8. (Supplementary Fig. 22), suggesting the same active sites for Li and Na storage in the sloping region. For a detailed quantitative analysis, temperature-programmed desorption coupled with mass spectrometry was employed to accurately determine the quantity of carbon defects, which include edges, vacancies and dislocations[26]. In Supplementary Fig. 23a,b, the total amount of CO and CO_2 from HCS-1,200 is higher than that from HCS-1,600, which is similar to the evolution tendency of H_2O and H_2. Considering the occupied area of edge carbon sites by a chemisorbed oxygen atom is 0.083 nm^2, the related active surface areas of HCSs can be calculated in Supplementary Fig. 23c. Assuming ions cover the entire active area, we successfully predict the sloping capacity in Fig. 3c, matching the experimental values and the 1.8 ratio of Li/Na storage. Elemental analysis for HCSs revealed that the content of heteroatoms such as oxygen is less than 1% (carbon: >99%), with limited capacity contribution (Supplementary Fig. 24).

Quantitative analysis for plateau region

For the plateau region, most of the previous reports explained pore filling or intercalation as the primary mechanism[20,35]. The possibility of an intercalation mechanism is further ruled out through the in situ Raman tests, ex situ X-ray diffraction and transmission electron microscopy (Supplementary Figs. 19 and 25). Besides, several investigations[39–41] have found hard carbons with a high plateau capacity (>300 mAh g^{-1}) that is unfeasible to be reached through intercalation. Then pore structures are considered to clarify the correlation with the plateau region. DFT analysis was carried out to interpret the microscopic origin of the storage process underlying the plateau capacity. A wedge-pore model, featured with edges, vacancies and pore structures, was built to mimic the typical microstructure of HCSs (Supplementary Fig. 26). The electrochemical process was simulated by filling the wedge-pore with Li and Na atoms in energy competing positions and performing geometrical and energy optimizations. On the basis of the lowest enthalpy path in Fig. 3d, we can obtain the Li and Na voltage profiles, shown in Fig. 3e.

https://doi.org/10.1038/s41560-023-01414-5

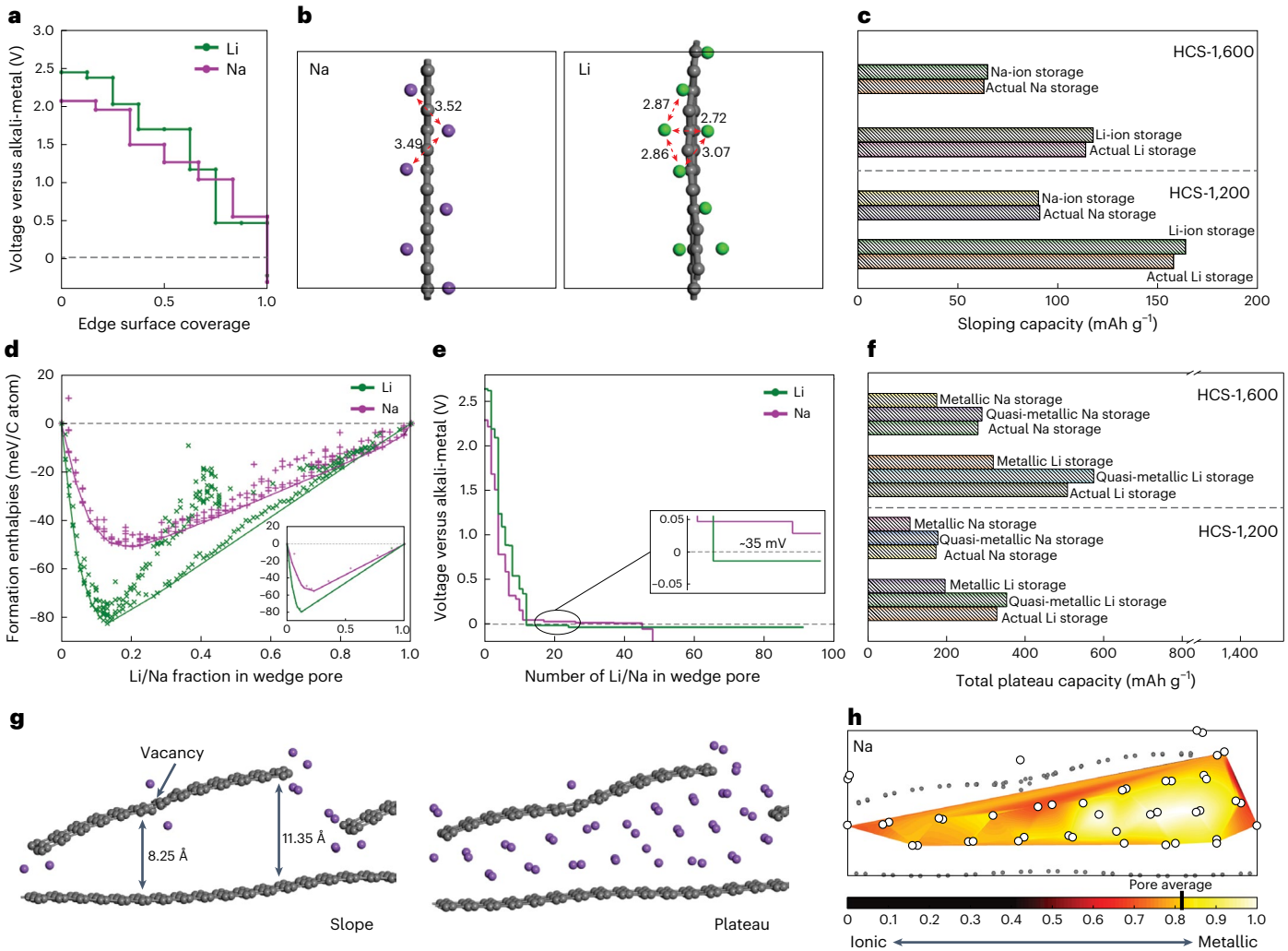

Fig. 3 | Quantitative Na storage mechanism analysis. a, DFT calculated voltage profile of Li and Na edge surface adsorption. **b**, Configurational geometry of optimized Li and Na adsorption on edge surfaces. Purple spheres indicate Na, green spheres indicate Li and grey spheres with stick connections represent C connected and forming the edges of a graphene sheet. **c**, Comparison between the experimental sloping capacities and calculated sloping capacities of HCSs for Li and Na storage based on the active surface area data (temperature-programmed desorption coupled with mass spectrometry). **d**, Convex hulls of the wedge-like pores. The inlet represents the second relaxation step as described in Methods. **e**, DFT calculated voltage profiles of the wedge-pore lithiation and sodiation, inlets of the second relaxation step and zoom-in regions close to the plateau are present. **f**, Comparison between the experiment plateau capacities and calculated plateau capacities based on simulative processes of Li or Na storage in the wedge-pore model. The breakpoint is designed to keep the capacity value display under different circumstances on the same *x* axis. **g**, Stable sodiation phases at the end of the sloping region (left) and at the voltage plateau (right). **h**, Valence electron heat map through Bader charge analysis of the sodiated pore. The figure quantifies how much electron density has been donated from Na to the carbon matrix. A value of 1 (white colour) indicates that Na is present as an atom keeping 100% of its valence electron density, and a value of 0 (black colour) indicates that Na has donated 100% of its valence to the carbon matrix, thus is present in an ionic form.

Sodiation initiates on defects consisting of edges and vacancies, as expected from previous discussions, to result in the sloping voltage region (Fig. 3g). Further, the sodiation reaction process moves to the pore-filling stage, and each graphene sheet of the inner carbon surface is in contact with 1–2 Na layers. Bader charge analysis through DFT calculations reveals the valence electron transfer distribution in the fully sodiated wedge pore, where on average, and inside the pore, 20% of the valence electron density is donated to the carbon matrix (Fig. 3h), supporting that Na is present in a quasi-metallic state, consistent with density of states calculations of similar pore configurations[42]. The reader can additionally observe that near the vacancy and edges, a more significant portion of electron density is donated to the carbon matrix whereas the inner Na is almost neutral, in line with the literature[42,43]. Li exhibits a similar reaction pathway, with the only difference being that more Li fits in the same pore size (Supplementary Fig. 27). In situ solid-state nuclear magnetic resonance (NMR) experiments further identified the Knight shift, capturing a quasi-metallic Na peak shift at approximately 761 ppm, compared with the ~1,135 ppm of the Na-metal signal. This denotes partial electron transfer, as shown in Supplementary Fig. 28, aligning with findings from previous NMR investigations[25,43–45]. The quasi-metallic state of Li or Na in the closed pore was further established experimentally using biphenyl-dimethoxyethane chemical probes (Supplementary Fig. 20) and electron paramagnetic resonance tests (Supplementary Fig. 30). No complete metallic state was detected, indicating a high safety of Li and Na in the closed pore. Li and Na can find an open path towards the inside of the nanopores through site defects as revealed by in situ Raman tests (Supplementary Fig. 20).

Combined with the above experimental tests and further simulations (Supplementary Fig. 31), we found that the Li and Na exist in an amorphous, quasi-metallic solid state inside the closed nanopores. Average Na–Na and Li–Li distances from the DFT-optimized

https://doi.org/10.1038/s41560-023-01414-5

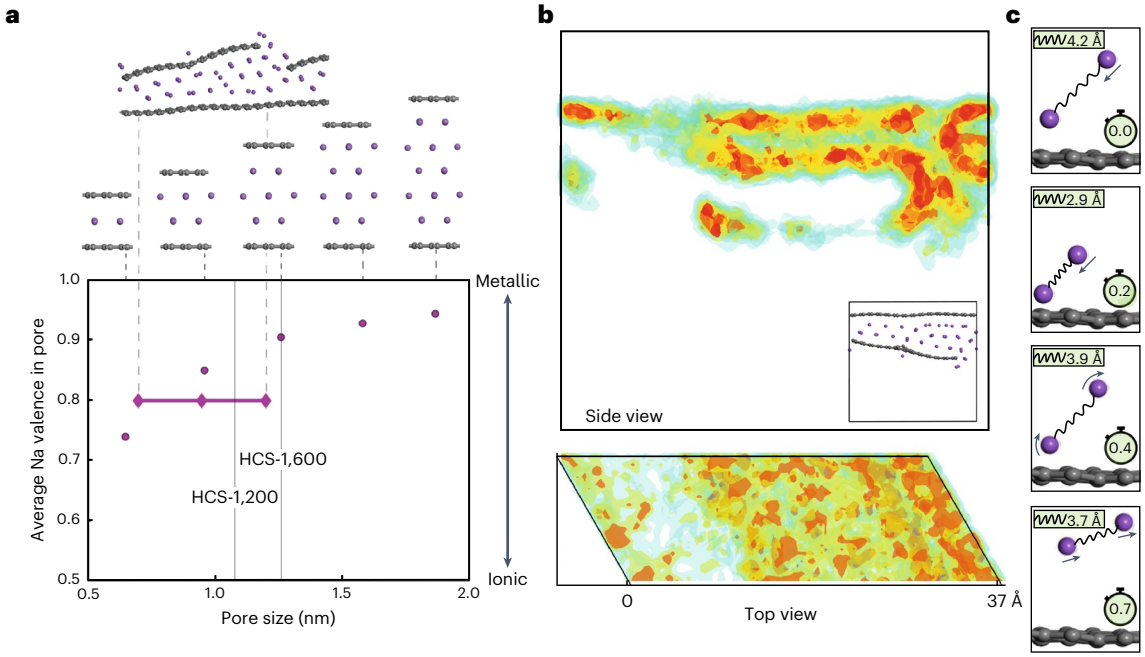

Fig. 4 | Wedge nanopore kinetics. a, Average Na valence charge in pore versus pore size distribution as calculated for the Na-in-pore system presented in Supplementary Fig. 32; the average Na valence charge for the wedge pore as calculated in Fig. 3h is plotted as well in comparison with the average experimental pore size of HCS-1,200 and HCS-1,600. **b**, Na density plot over the 18 ps MD simulation at 600 K depicted from the side and top view. The Na density is interconnected, covering the whole pore region, revealing that Na can quickly diffuse, being able to access all parts of the nanopore within small time frames. **c**, Depiction of correlated diffusion in the pore. The spring subplot refers to the Na–Na distances in Å, and the timer counts in ps (Supplementary Video 1).

wedge-pore model structures were predicted at 3.57 and 2.84 Å, respectively. According to the previous pore analysis, there is a positive correlation between the plateau capacity and the volume of closed pores. We can successfully predict the Li and Na specific capacity from the closed pore volume (experimental values) and the above-calculated distances, explaining the origin of the high-capacity voltage plateau. (Fig. 3f).

Moreover, the calculated voltage profiles in Fig. 3e masterfully capture the experimentally determined difference in voltage (30–40 mV) between the alkali metals, showing Na at a slightly positive potential of ~38 mV from Li, which ends up at negative potentials, rationalizing the absence of a Li plateau without overdischarge. To understand this difference in depth, we computationally explore surface energies, plating and interface contact potentials between Li or Na and graphene. To do so, we compare the energetics of Li and Na layers in the vacuum (exposed metallic surfaces) with encapsulated Li and Na layers within graphene sheets (no exposed surfaces) (Supplementary Fig. 32 and Supplementary Table 1). We observe that the Li and Na layers–graphene interfaces stabilize the system, raising the voltage by decreasing the energy penalty related to exposed surfaces. This effect is calculated to be more substantial for Na than for Li, consistently resulting in slightly higher potentials for the Na plateau. Thus, the relative stability of the lithiated and sodiated phases (Supplementary Figs. 32–34) is the consequence of the lower interface energy between Li or Na and the graphene walls compared to exposed surfaces. This observation is the key to understanding the difference in the voltage versus the alkali-metal potential between Li and Na, and it plays a dominant role in the storage capacity of the plateau region, enabling Na storage in slightly positive voltages versus Na metal, which improves the resilience against polarization, thereby reducing the risk of Na plating and facilitating fast charging[30]. Likewise, the system prefers to form filled pores, where the graphene walls wet the Li and Na exposed surfaces to take away the energy penalty. We additionally use the calculated potentials of the state of the filled pore to indicate the process of Li and Na layering in the nanopores absent from plating (Supplementary Fig. 34).

The above discussion hints towards an optimal pore size for the electrochemical process. Large nanopores will permit the nucleation of Li or Na to such a degree that the exposed surface penalty will result in overpotentials, causing the voltage to drop to the cut-off point before the pore-filling mechanism can stabilize the configuration by establishing the hard carbon–Li or Na interface contacts. Thus, the competition between nucleation and surface coverage suggests that there should be an optimum pore size (~1 nm) for the storage mechanism, consistent with what was experimentally determined[22]. Moreover, the DFT calculations indicate that there are 2–3 layers (Na) or 3–4 layers (Li) in the pore, similar to the UPD mechanism on metal substrates. In the case of UPD, the deposited layer is in a quasi-metallic state, and there is an interaction between the base and adsorbed layer that lowers the energy[46], consistent with our DFT calculations. It is also intricately linked to the difference in the work functions of adsorbate (Li and Na) and substrate (C), with the former possessing a smaller work function than that of the latter (Supplementary Fig. 35), causing the partial charge of the adatoms. Note that UPD is not limited to monolayer adsorption, as demonstrated by investigations that report adsorption of 1.5–2 atomic layers[47]. In hard carbon, the UPD-like mechanism requires substrate voids enabling full enclosure (minimal exposed surfaces) of Li and Na fillings and partial electron transfer to the substrate, thus achieving the least negative deposition potentials. The electrochemical curves (plateau region) of Li or Na in hard carbon are similar to the adsorption isotherm of UPD[48].

The quasi-metallic state of Na inside the pore has implications both on the optimum pore size, as discussed above, and the kinetics. This is because larger pores are expected to induce higher metallic states, slowing down the (dis)charge process. Further, we quantitatively show with DFT calculations how the average Na valence charge depends on pore size in Fig. 4a, enhancing our insights on design criteria for hard carbon systems. Experimentally, the HCS-1,200 (pore size: ~1.08 nm) shows a better fast-charging property than the HCS-1,600 (pore size: ~1.26 nm) in line with the above discussion. The result also implies that

keeping as many relatively small closed nanopores as possible is an effective strategy for large and fast storage because relatively large closed pores would induce a stronger metallic state of Na storage with lower average potential, which easily suffers from the risk of plating during fast charging, and the Na insertion process is also unstable with poor reversibility[49].

Wedge nanopore kinetics

We also performed phase-field modelling simulations to gain extra insights into the kinetics of Na–hard carbon system. The phase-field framework is well applied to the simulation of LIBs and can provide insights into the mechanism regulating battery performance and guide towards optimization[50–55]. Our mesoscale model is based on modifying an established open-source code[3] (details in Methods) and implementing the Na insertion mechanisms in hard carbon. Our model captures the physics of the sodiation mechanism as explored computationally with ab initio calculations, showing a gradually decreasing, high-voltage region followed by a low-voltage plateau.

In the results presented in Supplementary Figs. 36 and 37, we break down our system's overpotential contributions, initiating a discussion on the importance of nanostructure optimization affecting the reaction kinetics and Na concentration. A combination of good particle size and improved nanoporosity of the particles enhances the exchange current density and prevents Na from reaching a critical mass and initiating plating, which is vital for NIB optimization.

We further evaluated whether the Na layering in the wedge pore poses a kinetic restriction in the nanoscale. Ab initio molecular dynamics simulations are utilized as a qualitative indicator due to the large size of the wedge-pore model (Methods). We examine the pore at 50% capacity, representing the kinetics in the middle of the formation of the completely sodiated phase, where there is an adequate amount of space for Na movement. Na appears mobile in very short timescales (~18 ps); the Na density plot (Fig. 4a) reveals excellent interconnectivity as Na can access every part of the wedge pore. This observation hints towards a relatively flat energy landscape for the wedge-pore geometry, which is the driving force for diffusion. Under these conditions, even though Na prefers to group, it can quickly move in a fluid-like motion within the pore. Further, under these conditions and short time frames (1–3 ps), two Na atoms can correlate (form a dipole) and diffuse in a singular correlated motion (Fig. 4b), as depicted in Supplementary Video. The correlated jumps are expected as there is no screening among the Na atoms in the current configurational geometry, confirming that pair Li or Na migration facilitates fast diffusion[56,57].

Conclusions

In retrospect, the accurate assessment of the Li and Na capacity in hard carbon, including the hidden capacity below 0 V, and the importance of the hard carbon–Li and Na surface contact, provides a quantitative and unified explanation of the storage mechanism. A UPD-like behaviour is put forward, rationalizing the excellent kinetics of hard carbon and fast charging. These insights promote the practical design of future carbon anode with predictable electrochemical behaviour to approximate the optimal fast-charging properties of NIBs towards grid energy storage application. In this work, we pay more attention to achieving the industrial-level parameters of cell fabrication and the electrochemical performance of assembled NIBs. Compared with the literature concerning NIB technologies, which is summarized in Supplementary Table 3, to the best of our knowledge, this Ah-level $Na(Cu_{1/9}Ni_{2/9}Fe_{1/3}Mn_{1/3})O_2$// HCS-1,200 cylindrical cell is among the best fast-charging technologies with one of the shortest charging times (~9 min) and one of the longest cycling lives (~3,000 cycles) under the high charging rate using the highest mass loading of active materials (7–8 mg cm^{-2}) with high areal capacity of ~2.2 mAh cm^{-2}.

Methods

Materials synthesis

HCS samples were prepared by hydrothermal method and subsequent pyrolysis. Typically, a 2 M sucrose aqueous solution (obtained from Alfa) was positioned in a Teflon-lined stainless-steel autoclave. The hydrothermal carbonization was executed at a temperature of 200 °C for 12 h followed by repeated washing processes with dilute hydrochloric acid and deionized water. Further high-temperature treatment was carried out at 1,200 °C and 1,600 °C for 2 h in a tube furnace under argon flow. The grinded samples were abbreviated as HCS-1,200 and HCS-1,600, respectively.

Electrochemical measurements

Composite electrodes were crafted by compressing a blend of active materials and sodium alginate, with a weight ratio of 9:1, in deionized water as the solvent, and then applying the mixture onto Cu foil. The active materials' mass loading was meticulously maintained between 4 and 5 mg cm^{-2}. For electrochemical testing of the carbon materials, CR2032 coin-type cells were constructed. Pure lithium/sodium foil, a 1 M (mol l^{-1}) $LiPF_6$/$NaPF_6$ solution in ethyl carbonate (EC) and dimethyl carbonate (DMC) (at a 1:1 volume ratio) and glass fibre were employed as the counter electrode, electrolyte and separator, respectively. All fabrication procedures were carried out in an argon-saturated glovebox. Discharge and charge tests were conducted using a Land BT3001A battery test system, cycling within various voltage ranges at a current density of 15 mA g^{-1}.

The Na-ion Ah-level full cells were constructed using HCS-1,600/HCS-1,200 as anode materials and O3-$Na(Cu_{1/9}Ni_{2/9}Fe_{1/3}Mn_{1/3})O_2$/$Na_3(VOPO_4)_2F$ as cathode materials. The 26700-type cylindrical cells (capacity is ~3 Ah and energy density is ~110 Wh kg^{-1}) using 1 M $NaPF_6$ in EC, propylene carbonate and diethyl carbonate (1:1:1 in volume) as electrolyte were assembled and their temperature changes were monitored by a thermal imager (FOTRIC 289). The capacity ratio of anode to cathode was ~1.1 for the 26700-type cylindrical Na-ion full cells based on the HCS-1,200 (the areal capacity can achieve ~2.2 mAh cm^{-2}). The mass loading of anode was ~7–8 mg cm^{-2}. The power density of 6.5 C is ~600 W kg^{-1}. The thickness of double-sided coated HCS-1,200 anodes has reached ~170 μm after cold pressing process. Both cathode and anode use aluminium foil as current collector, and the polyolefin separator was used. Composite electrodes were fabricated by compressing active materials, binder and conductive carbon at a weight ratio of 95:3:2. The electrolyte filling processes were carried out in a dry room at −50 °C dew point. The charge and discharge tests of full cells were performed on the Neware battery test system (CT-4008). The HCS-based full cells were charged and discharged between 1.5 and 4 V. Note that it is constant current charging to 100% state of charge without a constant voltage step. The cells were placed in a ~25 °C environment chamber.

Materials characterization

The morphologies of the carbons were examined using scanning electron microscopy (Hitachi-S4800), and transmission electron microscopy images were captured using a JEOL 2100 F field emission device. Structural characterizations were conducted using an X'Pert Pro MPD X-ray diffractometer (D8 Bruker) with Cu-Kα radiation, in a scan range (2θ) of 10°–60°. Raman spectra, ranging between 1,000 and 1,800 cm^{-1}, were collected using an NRS-5100 spectrometer (JASCO) with a 532 nm diode-pumped solid-state laser.

Information regarding pore structure was acquired through nitrogen adsorption/desorption experiments at 77 K using a Micrometrics ASAP 2460 apparatus and SAXS/wide angle X-ray scattering from a Xenocs Nano-InXider with a Cu-Kα source. Skeletal density data were gathered using an AccuPyc II 1340 analyser with helium as the analysis gas. Elemental analysis was conducted using a Vario Micro Cube element analyser. Active surface areas of the carbons were determined through temperature-programmed desorption (AutoChem II 2920)

paired with mass spectrometry (HPR-20 EGA). The test procedure was the same as that reported in the previous literature[26]. The biphenyl and dimethoxyethane solution was prepared by dissolving 1.54 g biphenyl into 10 ml dimethoxyethane. The chemical states of inserted Li or Na were determined by electron paramagnetic resonance using JEOL JES-FA200 ESR Spectrometer with the microwave frequency of 9,068 MHz. ^{23}Na magic angle spinning solid-state NMR measurements were carried out in a Bruker 500 MHz spectrometer (11.7 T). A spin speed of 13 kHz was used and the pulse length was 0.62 µs. The chemical shifts were referenced to 1 M NaCl in water as 0 ppm.

For the ex situ measurements, the electrode disassembled from the coin cell in an argon-filled glovebox was washed in DMC repeatedly followed by a drying processing in an Argon-filled transferred tube. The in situ Raman spectra were also recorded with an NRS-5100 spectrometer (JASCO) using a 532 nm diode-pumped solid-state laser between 1,000 and 1,800 cm^{-1} in combination with a Land 2001A battery testing system. Specially designed optical cells, which have central holes to allow the laser beam to pass through to the surface of HCS, were assembled. Cells were tested at the current density of 15 mA g^{-1} at ambient temperature. The data of second discharging process were collected to avoid the influence of solid electrolyte interphase. Na-metal|1 M $NaPF_6$ in EC:DMC|hard carbon cells (in a plastic cell capsule suitable for in situ NMR measurements) with a conventional non-aqueous carbonate electrolyte solution were assembled in the glovebox and studied by in situ ^{23}Na NMR. Solid-state NMR measurements were performed on a Bruker Ascend 500 magnet (11.7 T) equipped with a Bruker NEO console operating at a ^{23}Na resonance frequency of 132.37 MHz. In situ static ^{23}Na NMR experiments were performed at room temperature with an NMR Service ATMC operando NMR probe, and the electrochemical cell was simultaneously controlled by a portable Maccor battery testing system. During the 1D static ^{23}Na NMR measurements, the cells were first discharged to 0 V versus Na^+/Na and charged till 2 V at C/10. Single-pulse measurements with a π/2 pulse of 3 µs and recycle delay of 0.05 s was applied to acquire the 1D static spectrums each spectrum comprising of 7,168 scans.

Computations

First-principles calculations are performed with the Vienna ab initio simulation package[58]. The Perdew–Burke–Ernzerhof[59,60] exchange-correlation functional, and the projector-augmented wave approach[61] were employed. To account for Van der Walls interactions we applied the DFT-D3 corrections. The energy and force convergence criteria for structure relaxation were set to 10^{-4} eV and 10^{-3} eV Å^{-1}, respectively. Single and bilayer graphene sheet calculations were performed using slab configurations with a vacuum of at least 15 Å, where the cut-off energy and k-point grid were selected to be 500 eV and 7 × 7 × 1, respectively. For the wedge-pore system, the cut-off energy and k-point grid were reduced down to 400 and 3 × 3 × 1. This calculation occurred in two subsequent relaxation steps: first, for each configuration at each concentration, the carbon matrix was locked in position, allowing only Na to relax. Next, the configurations on the convex line (most stable configurations) were re-optimized with both Na and the carbon matrix able to relax (Supplementary Fig. 38). The enthalpies of formation (H) and average voltages (V) were obtained based on the calculated energies according to the following formulas[62–64]:

$$H = E_{M_xC} - xE_{M_{max}C} - (1-x)E_C \quad (1)$$

$$V = \frac{-\left[E_{M_xC} - (x-y)E_M - E_{M_yC}\right]}{(x-y)e} \quad (2)$$

where E_{MC}, E_C, E_M and e represent the total energies of Li or Na in the carbon matrix, carbon matrix, the Na or Li atom in the metallic crystal form and the electron charge, respectively.

Ab initio molecular dynamics calculations were performed using 400 eV and 1 × 1 × 1 cut-off energy and k-point mesh, respectively. All simulations were performed within the canonical computational ensemble computational ensemble and utilized a 2 fs time step and a 2.5 ps equilibration time. The y axis of the wedge pore was doubled to avoid self-interaction between the Na atoms leading to a 1 × 2 × 1 supercell configuration of the structure presented in Supplementary Fig. 26 with dimensions 37 × 14.8 × 30 Å with a total of 334 C and 52 Na diffusing atoms. At the end of the discharge process, all pore positions are occupied, and the pore is completely filled. Here we selected to study the pore at 50% capacity. In this way, we can determine whether Na atoms can move sufficiently fast in the nanopore environment within the time frame of the ultra-high currents measured herein experimentally. Due to the large size of the realistic investigated pore, a quantitative analysis was not feasible, obtaining a simulation time of 18 ps at 600 K.

We build our mesoscale model in an advanced, open-source LIBs phase-field framework called MPET[50–55]. We modified the framework to include the kinetics of NIBs. To model the system, we fit the average open circuit voltage (OCV) data between charging and discharging to obtain the chemical potential dependence on concentration. The fitting was necessary because even if the ab initio simulations provided a great explanation of the experimental results, the disordered nature of the material would require a disproportional number of computations, while instead fitting the OCV can immediately provide a good model.

From the fitting of the voltage hysteresis between charge and discharge, it was possible to obtain a non-monotonic (phase separation) zone of the chemical potential. This region corresponds to the filling fractions 0.57–0.92, which is consistent with the observed phase separation and the convex hull of the ab initio simulations. To complete the phase-field model, the gradient penalty term κ was included, and considering the similarities, the same value used by Smith et al.[52] to model the lithiation of graphite was used so that $\kappa = 4 \times 10^{-7}$ J m^{-1}. The rest of the parameters can be found in Supplementary Table 3 of the supporting information which was estimated from direct measurements, including impedance results and so on. The exchange current density, denoted as k_0, is considered as an effective exchange current density that takes into account the nanoporous surface of particles.

The core equation governing the physics and kinetics of the single particle are:

$$\mu_{HC} = \mathrm{OCV} \quad (3)$$

$$i(c) = \frac{k_0 a_O^{1-\alpha} a_{HC}^{\alpha}}{\gamma_{HC}^{\ddagger}} \left(e^{-\frac{ae\eta}{k_B T}} - e^{\frac{(1-a)e\eta}{k_B T}}\right) \quad (4)$$

$$F = -\frac{D_0}{k_B T} c \nabla \mu_{HC} \quad (5)$$

where μ_{HC} is the chemical potential of the hard carbon; i is the current; F is the flux inside the particle; c is the normalized concentration; D_0 is the self-diffusion coefficient; T is the temperature; k_B is the Boltzmann constant; α is the reactor symmetry factor; k_0 is the reaction rate constant per unit area; e is the elementary charge; a_O is the activity of the oxidized state, which also includes the activity of the electron participating in the reaction; a_{HC} is the activity of hard carbon; η is the charge transfer overpotential ($e\eta = \mu_{HC} - \mu_O$) and $\gamma_i^{\ddagger} = \frac{1}{(1-c)^{0.5}}$ is the activity coefficient of the transition state. For the last dependency, a square root of the vacancy dependence was chosen to assume a less important effect of the filling fraction on the reaction rate due to the amorphous nature of the material. For comparison, Li–graphite simulations were conducted based on the work of Torchio et al.[65]. A thorough and complete presentation of the porous electrode model and its capabilities is presented in the work of Smith et al.[52]. In the latter part of the

Supplementary Information, we provide more details on the sequence and structural characteristics of our simulations (Supplementary Figs. 39–42).

Data and materials availability

The data supporting the findings of this study are available within the article and its Supplementary Information files.

References

1. Kang, B. & Ceder, G. Battery materials for ultrafast charging and discharging. *Nature* **458**, 190–193 (2009).
2. Lin, M.-C. et al. An ultrafast rechargeable aluminium-ion battery. *Nature* **520**, 324–328 (2015).
3. Liu, Y., Zhu, Y. & Cui, Y. Challenges and opportunities towards fast-charging battery materials. *Nat. Energy* **4**, 540–550 (2019).
4. Attia, P. M. et al. Closed-loop optimization of fast-charging protocols for batteries with machine learning. *Nature* **578**, 397–402 (2020).
5. Zhang, W. et al. Kinetic pathways of ionic transport in fast-charging lithium titanate. *Science* **367**, 1030 (2020).
6. Cai, W. et al. A review on energy chemistry of fast-charging anodes. *Chem. Soc. Rev.* **49**, 3806–3833 (2020).
7. Li, Y., Lu, Y., Adelhelm, P., Titirici, M.-M. & Hu, Y.-S. Intercalation chemistry of graphite: alkali metal ions and beyond. *Chem. Soc. Rev.* **48**, 4655–4687 (2019).
8. Sun, H. et al. Three-dimensional holey-graphene/niobia composite architectures for ultrahigh-rate energy storage. *Science* **356**, 599–604 (2017).
9. Griffith, K. J., Wiaderek, K. M., Cibin, G., Marbella, L. E. & Grey, C. P. Niobium tungsten oxides for high-rate lithium-ion energy storage. *Nature* **559**, 556–563 (2018).
10. Jin, H. et al. Black phosphorus composites with engineered interfaces for high-rate high-capacity lithium storage. *Science* **370**, 192–197 (2020).
11. Liu, H. et al. A disordered rock salt anode for fast-charging lithium-ion batteries. *Nature* **585**, 63–67 (2020).
12. Chen, K.-H. et al. Enabling 6C fast charging of Li-ion batteries with graphite/hard carbon hybrid anodes. *Adv. Energy Mater.* **11**, 2003336 (2021).
13. Komaba, S. et al. Electrochemical Na insertion and solid electrolyte interphase for hard-carbon electrodes and application to Na-ion batteries. *Adv. Funct. Mater.* **21**, 3859–3867 (2011).
14. Li, Y. et al. Regulating pore structure of hierarchical porous waste cork-derived hard carbon anode for enhanced Na storage performance. *Adv. Energy Mater.* **9**, 1902852 (2019).
15. Pu, X. et al. Recent progress in rechargeable sodium-ion batteries: toward high-power applications. *Small* **15**, 1805427 (2019).
16. Liu, T. et al. Exploring competitive features of stationary sodium ion batteries for electrochemical energy storage. *Energy Environ. Sci.* **12**, 1512–1533 (2019).
17. Usiskin, R. et al. Fundamentals, status and promise of sodium-based batteries. *Nat. Rev. Mater.* **6**, 1020–1035 (2021).
18. Rudola, A., Wright, C. J. & Barker, J. Communication—surprisingly high fast charge volumetric capacities of hard carbon electrodes in sodium-ion batteries. *J. Electrochem. Soc.* **168**, 110534 (2021).
19. Dahn, J. R., Zheng, T., Liu, Y. & Xue, J. S. Mechanisms for lithium insertion in carbonaceous materials. *Science* **270**, 590–593 (1995).
20. Saurel, D. et al. From charge storage mechanism to performance: a roadmap toward high specific energy sodium-ion batteries through carbon anode optimization. *Adv. Energy Mater.* **8**, 1703268 (2018).
21. Moon, H. et al. Assessing the reactivity of hard carbon anodes: linking material properties with electrochemical response upon sodium- and lithium-ion storage. *Batteries Supercaps* **4**, 960–977 (2021).
22. Kubota, K. et al. Structural analysis of sucrose-derived hard carbon and correlation with the electrochemical properties for lithium, sodium, and potassium insertion. *Chem. Mater.* **32**, 2961–2977 (2020).
23. Stevens, D. A. & Dahn, J. R. The mechanisms of lithium and sodium insertion in carbon materials. *J. Electrochem. Soc.* **148**, A803 (2001).
24. Alvin, S. et al. Revealing the intercalation mechanisms of lithium, sodium, and potassium in hard carbon. *Adv. Energy Mater.* **10**, 2000283 (2020).
25. Stratford, J. M. et al. Correlating local structure and sodium storage in hard carbon anodes: insights from pair distribution function analysis and solid-state NMR. *J. Am. Chem. Soc.* **143**, 14274–14286 (2021).
26. Ghimbeu, C. M. et al. Insights on the Na+ ion storage mechanism in hard carbon: discrimination between the porosity, surface functional groups and defects. *Nano Energy* **44**, 327–335 (2018).
27. Mu, L. et al. Electrochemical properties of novel O3-$NaCu_{1/9}Ni_{2/9}Fe_{1/3}Mn_{1/3}O_2$ as cathode material for sodium-ion batteries. *Energy Storage Sci. Technol.* **5**, 324 (2016).
28. Heenan, T. M. M. et al. Mapping internal temperatures during high-rate battery applications. *Nature* **617**, 507–512 (2023).
29. Wang, C.-Y. et al. Fast charging of energy-dense lithium-ion batteries. *Nature* **611**, 485–490 (2022).
30. Li, Y., Lu, Y., Chen, L. & Hu, Y.-S. Failure analysis with a focus on thermal aspect towards developing safer Na-ion batteries. *Chin. Phys. B* **29**, 048201 (2020).
31. Zhang, S. S. The puzzles in fast charging of Li-ion batteries. *Energy Environ. Mater.* **5**, 1005–1007 (2022).
32. Colclasure, A. M. et al. Electrode scale and electrolyte transport effects on extreme fast charging of lithium-ion cells. *Electrochim. Acta* **337**, 135854 (2020).
33. Logan, E. R. et al. Ester-based electrolytes for fast charging of energy dense lithium-ion batteries. *J. Phys. Chem. C.* **124**, 12269–12280 (2020).
34. Yang, X.-G. et al. Asymmetric temperature modulation for extreme fast charging of lithium-ion batteries. *Joule* **3**, 3002–3019 (2019).
35. Chen, D. et al. Hard carbon for sodium storage: mechanism and optimization strategies toward commercialization. *Energy Environ. Sci.* **14**, 2244–2262 (2021).
36. Cohn, A. P., Share, K., Carter, R., Oakes, L. & Pint, C. L. Ultrafast solvent-assisted sodium ion intercalation into highly crystalline few-layered graphene. *Nano Lett.* **16**, 543–548 (2016).
37. Bai, P. et al. Elucidation of the sodium-storage mechanism in hard carbons. *Adv. Energy Mater.* **8**, 1703217 (2018).
38. Sangavi, S., Santhanamoorthi, N. & Vijayakumar, S. Density functional theory study on the adsorption of alkali metal ions with pristine and defected graphene sheet. *Mol. Phys.* **117**, 462–473 (2019).
39. Zhao, C. et al. High-temperature treatment induced carbon anode with ultrahigh Na storage capacity at low-voltage plateau. *Sci. Bull.* **63**, 1125–1129 (2018).
40. Meng, Q. et al. Tuning the closed pore structure of hard carbons with the highest Na storage capacity. *ACS Energy Lett.* **4**, 2608–2612 (2019).
41. Kamiyama, A. et al. MgO-template synthesis of extremely high capacity hard carbon for Na-ion battery. *Angew. Chem. Int. Ed.* **60**, 5114–5120 (2021).
42. Youn, Y. et al. Nanometer-size Na cluster formation in micropore of hard carbon as origin of higher-capacity Na-ion battery. *npj Comput. Mater.* **7**, 48 (2021).
43. Stratford, J. M., Allan, P. K., Pecher, O., Chater, P. A. & Grey, C. P. Mechanistic insights into sodium storage in hard carbon anodes using local structure probes. *Chem. Commun.* **52**, 12430–12433 (2016).

44. Au, H. et al. A revised mechanistic model for sodium insertion in hard carbons. *Energy Environ. Sci.* **13**, 3469–3479 (2020).
45. Morita, R. et al. Combination of solid state NMR and DFT calculation to elucidate the state of sodium in hard carbon electrodes. *J. Mater. Chem. A* **4**, 13183–13193 (2016).
46. Herrero, E., Buller, L. J. & Abruña, H. D. Underpotential deposition at single crystal surfaces of Au, Pt, Ag and other materials. *Chem. Rev.* **101**, 1897–1930 (2001).
47. Huang, M. et al. In depth analysis of complex interfacial processes: in situ electrochemical characterization of deposition of atomic layers of Cu, Pb and Te on Pd electrodes. *RSC Adv.* **2**, 10994–11006 (2012).
48. Lee, H.-H., Wan, C.-C. & Wang, Y.-Y. Identity and thermodynamics of lithium intercalated in graphite. *J. Power Sources* **114**, 285–291 (2003).
49. Li, Q. et al. Sieving carbons promise practical anodes with extensible low-potential plateaus for sodium batteries. *Natl Sci. Rev.* **9**, nwac084 (2022).
50. Vasileiadis, A. et al. Toward optimal performance and in-depth understanding of spinel $Li_4Ti_5O_{12}$ electrodes through phase field modeling. *Adv. Funct. Mater.* **28**, 1705992 (2018).
51. de Klerk, N. J. J., Vasileiadis, A., Smith, R. B., Bazant, M. Z. & Wagemaker, M. Explaining key properties of lithiation in TiO_2-anatase Li-ion battery electrodes using phase-field modeling. *Phys. Rev. Mater.* **1**, 025404 (2017).
52. Smith, R. B. & Bazant, M. Z. Multiphase porous electrode theory. *J. Electrochem. Soc.* **164**, E3291 (2017).
53. Liu, K. et al. Electrochemical modeling and parameterization towards control-oriented management of lithium-ion batteries. *Control Eng. Pract.* **124**, 105176 (2022).
54. Ferguson, T. R. & Bazant, M. Z. Nonequilibrium thermodynamics of porous electrodes. *J. Electrochem. Soc.* **159**, A1967 (2012).
55. Cogswell, D. A. & Bazant, M. Z. Size-dependent phase morphologies in $LiFePO_4$ battery particles. *Electrochem. Commun.* **95**, 33–37 (2018).
56. Kühne, M. et al. Reversible superdense ordering of lithium between two graphene sheets. *Nature* **564**, 234–239 (2018).
57. Zou, Z. et al. Relationships between Na^+ distribution, concerted migration, and diffusion properties in rhombohedral NASICON. *Adv. Energy Mater.* **10**, 2001486 (2020).
58. Kresse, G. & Furthmuller, J. Efficiency of ab-initio total energy calculations for metals and semiconductors using a plane-wave basis set. *Comp. Mater. Sci.* **6**, 15–50 (1996).
59. Perdew, J. P., Burke, K. & Ernzerhof, M. Generalized gradient approximation made simple. *Phys. Rev. Lett.* **77**, 3865–3868 (1996).
60. Lee, S.-H., Kang, J.-H. & Kang, M.-H. Structural properties of semiconductors in the generalized gradient approximation. *J. Korean Phys. Soc.* **31**, 811 (1997).
61. Blöchl, P. E. Projector augmented-wave method. *Phys. Rev. B* **50**, 17953–17979 (1994).
62. Van der Ven, A., Aydinol, M. K., Ceder, G., Kresse, G. & Hafner, J. First-principles investigation of phase stability in Li_xCoO_2. *Phys. Rev. B* **58**, 2975–2987 (1998).
63. Wagemaker, M. et al. Thermodynamics of spinel Li_xTiO_2 from first principles. *Chem. Phys.* **317**, 130–136 (2005).
64. Aydinol, M. K., Kohan, A. F., Ceder, G., Cho, K. & Joannopoulos, J. Ab initio study of lithium intercalation in metal oxides and metal dichalcogenides. *Phys. Rev. B* **56**, 1354–1365 (1997).
65. Torchio, M., Magni, L., Gopaluni, R. B., Braatz, R. D. & Raimondo, D. M. Lionsimba: a matlab framework based on a finite volume model suitable for li-ion battery design, simulation, and control. *J. Electrochem. Soc.* **163**, A1192 (2016).

Acknowledgements

This work was supported by the National Key R&D Program of China (2022YFB2402500), National Natural Science Foundation of China (52122214 and 52072403), Youth Innovation Promotion Association of the Chinese Academy of Sciences (2020006), Jiangsu Province Carbon Peak and Neutrality Innovation Program (Industry tackling on prospect and key technology BE2022002-5), and financial support is greatly acknowledged from the Netherlands Organization for Scientific Research under the VENI grant number 18123 and VICI grant number 16122.

Author contributions

Y.X.L., M.W. and Y-S.H. designed this work, Y.Q.L. synthesized the carbon electrodes and carried out the electrochemical experiments and materials characterization, A.V. performed first-principle calculations, P.O. performed mesoscale phase-field modelling simulations and Q.Z., Q.M. and J.Z. prepared the 26700-type cells. Y.Q.L., A.V., Y.X.L., P.O., M.W. and Y.-S.H. wrote the paper. All the authors participated in analysis of the experimental data and discussions of the results and in preparing the paper.

Competing interests

Q.Z., Q.M., J.Z., X.Q. and Y.-S.H. are employed at HiNa Battery Technology Co. Ltd. The other authors declare no competing interests.

Additional information

Supplementary information The online version contains supplementary material available at https://doi.org/10.1038/s41560-023-01414-5.

Correspondence and requests for materials should be addressed to Yaxiang Lu, Marnix Wagemaker or Yong-Sheng Hu.

Peer review information *Nature Energy* thanks Gui-Liang Xu and the other, anonymous, reviewer(s) for their contribution to the peer review of this work.